bioRxiv preprint doi: https://doi.org/10.1101/2020.12.07.411462; this version posted December 7, 2020. The copyright holder for this preprint (which was not certified by peer review) is the author/funder, who has granted bioRxiv a license to display the preprint in perpetuity. It is made available under aCC-BY 4.0 International license.

A massively multi-scale approach to characterising tissue architecture by synchrotron micro-CT applied to the human placenta

W. M. Tun[1, †], G. Poologasundarampillai[2, †], H. Bischof[3], G. Nye[4], O. N. F. King[1], M. Basham[1,5], Y. Tokudome[6], R. M. Lewis[7], E. D. Johnstone[3], P. Brownbill[3, *], M. Darrow[8, *], and I. L. Chernyavsky[3,9, *]

[1]Diamond Light Source, Didcot OX11 0DE, UK.
[2]School of Dentistry, University of Birmingham, Birmingham B15 2TT, UK.
[3]Maternal and Fetal Health Research Centre, School of Medical Sciences, University of Manchester; MAHSC, St Mary's Hospital, NHS MFT, Manchester, M13 9WL, UK.
[4]University of Chester, Chester CH1 4BJ, UK.
[5]Rosalind Franklin Institute, Didcot OX11 0DE, UK.
[6]Osaka Prefecture University, Osaka 599-8531, Japan.
[7]University of Southampton, Faculty of Medicine, Southampton SO16 6YD, UK.
[8]SPT Labtech Ltd, Melbourn SG8 6HB, UK.
[9]Department of Mathematics, University of Manchester, Manchester M13 9PL, UK.

† These authors contributed equally to the work.
* Joint lead authors.
Correspondence emails: igor.chernyavsky@manchester.ac.uk; Michele.c.Darrow@gmail.com; Paul.Brownbill@manchester.ac.uk

Keywords: placenta, vascular tissue, computed tomography, machine learning, multi-domain segmentation, dual network flow, spatial statistics, stochastic geometry, U-Net, perfusion, contrast agent

Summary: Using the human placenta as an example, this study brings together sophisticated sample preparation protocols, advanced 3D X-ray imaging, and robust, validated machine-learning segmentation techniques to provide massively multi-scale and multi-domain insights on vascular-rich organ morphology and function.

ABSTRACT

Multi-scale structural assessment of biological soft tissue is challenging but essential to gain insight into structure-function relationships of tissue/organ. Using the human placenta as an example, this study brings together sophisticated sample preparation protocols, advanced imaging, and robust, validated machine-learning segmentation techniques to provide the first massively multi-scale and multi-domain information that enables detailed morphological and functional analyses of both maternal and fetal placental domains. Finally, we quantify the scale-dependent error in morphological metrics of heterogeneous placental tissue, estimating the minimal tissue scale needed in extracting meaningful biological data. The developed protocol is beneficial for high-throughput investigation of structure-function relationships in both normal and diseased placentas, allowing us to optimise therapeutic

bioRxiv preprint doi: https://doi.org/10.1101/2020.12.07.411462; this version posted December 7, 2020. The copyright holder for this preprint (which was not certified by peer review) is the author/funder, who has granted bioRxiv a license to display the preprint in perpetuity. It is made available under aCC-BY 4.0 International license.

approaches for pathological pregnancies. In addition, the methodology presented is applicable in characterisation of tissue architecture and physiological behaviours of other complex organs with similarity to the placenta, where an exchange barrier possesses circulating vascular and avascular fluid spaces.

I. INTRODUCTION

Understanding complex vascular-rich organs such as the placenta has traditionally necessitated the adoption of multiple parallel imaging-based approaches, which are applied correlatively to gain a structural and functional understanding of the tissue. These approaches generally require balancing resolution with sample volume. Structural analyses of placental vessels from whole organ or single villous branches have been conducted using multiple imaging modalities (*1, 2*) including CT angiography (*3*), micro-CT (*4, 5*), confocal laser scanning microscopy (*6*) and fluorescent CLSM (*7*). Each of these methods has positives and negatives associated with it, however, none of them provide access to 3D micro-structures *in situ*, at high enough resolution to resolve the blood vessels, or functional units of the placenta, and still provide contextual information of the various parts of the tissue.

Segmenting biological image data is a major challenge due to the structural complexity and intra/inter sample heterogeneity (*8, 9*). Manual segmentation is commonly used for biological data segmentation, however, as the number and size of datasets increases this approach has become increasingly impractical (*10*). Thus, an auto or semi-automatic segmentation algorithm with high accuracy is required for high throughput segmentation of biological structure.

As one of the most complex vascular organs of the human body, the placenta is a well-suited model system for development of 3D imaging pipelines. The human placenta is an exchange organ with a large surface area of the feto-maternal interface packed in a relatively small volume, with the total length of the feto-placental vascular network of over 550 km (*11*). Its tightly integrated structural constituents span the spatial range from $\sim 10^{-6}$ to 10^{-1} m, necessitating a truly massive multi-scale imaging modality. Thus, new experimental and theoretical approaches are needed to bridge the microstructure of the placental exchange barrier and its macroscopic organ-level function, including the three-dimensional

bioRxiv preprint doi: https://doi.org/10.1101/2020.12.07.411462; this version posted December 7, 2020. The copyright holder for this preprint (which was not certified by peer review) is the author/funder, who has granted bioRxiv a license to display the preprint in perpetuity. It is made available under aCC-BY 4.0 International license.

characterisation of the mesoscopic (in the range of ~ 0.1 – 1 mm) tissue domain (*1, 11*).

In this study, synchrotron X-ray imaging is used in combination with various sample processing conditions, including tissue contrast agents, vascular cast resins, fixation and embedding methods to generate high resolution massively multi-scale datasets of the human placenta. We then apply machine learning-based segmentation techniques for robust and efficient decomposition of maternal and fetal micro-domains in the large (≈ 8 mm^3) mesoscopic datasets. Finally, spatial statistics and flow simulations of the feto-placental vascular network and associated intervillous porous space of the placental tissue are presented, and the results are validated against other modalities such as traditional 2D stereology analysis and *in vivo* magnetic resonance imaging.

The developed protocols for 3D multi-domain characterisation of tissues presented here, using the human placenta as an example, will enable more direct hypothesis-testing of the structure–function relationship in other organs where there are complex physiological fluidic / exchanger systems such as in the kidney, lung, lymphatics, spleen, central nervous system, gut, bone-marrow and in wound healing and tumour biology.

II. RESULTS

A. Morphological study of mesoscopic placental tissue

(i). Comparative analysis of tissue preparation (fixation, perfusion, staining and dehydration/embedding) for X-ray micro-tomography of complex soft tissues

Preparation of placental specimens for synchrotron micro-CT requires careful fixation, perfusion, staining and dehydration/embedding (Figure S1). Here we apply and qualitatively evaluate various specimen preparation methods to successfully image the complex architecture of human placenta (Figure S2). Tissue zinc-based fixative Z7 provides tissue contrast when in-line phase contrast synchrotron imaging is performed (Figure S2). It is possible to observe various placental architectures in Figure S2A,D, including a well resolved

bioRxiv preprint doi: https://doi.org/10.1101/2020.12.07.411462; this version posted December 7, 2020. The copyright holder for this preprint (which was not certified by peer review) is the author/funder, who has granted bioRxiv a license to display the preprint in perpetuity. It is made available under aCC-BY 4.0 International license.

trophoblast shell, blood vessels, capillaries and red blood cells. It is also possible to observe parts of the stroma. From here, a machine-learning algorithm (U-Net) can be applied to segment the intervillous space. Additional staining with phosphotungstic acid (PTA) further enhances the contrast for stroma (Figure S2F) making it segmentable. However, the complex 3D vascular network cannot be segmented from these images alone. Resin infiltration casting of the fetal villi network gives sufficient contrast and phase difference (Figure S2B,E – Yasuaki's and Figure S2C – Batson's) to enable its segmentation. Batson's contrast agent penetrates deeply into the fetoplacental circulation (Figure S2C) but shrinks inside larger vessels and possibly over-inflates smaller vessels, due to the high exertion force needed to infuse the resin via the fetal arterial cannula. Yasuaki's resin is less viscous than Batson's and shrinks less, thereby likely better preserving vessel diameters. Both agents give good contrast to highlight the fetal lumen (Figure S2B,C). The viscosity of both Batson's and Yasuaki's reagents make them unfavourable for infusion into the intervillous space, since filling is incomplete. Whilst, the 1% PTA solution used to stain tissue has low viscosity and so infiltrates into the intervillous space but takes several days (3 days for an 8 mm^3 sample) to provide good contrast and signal-to-noise.

Extent of tissue processing influences final architecture. Ethanol dehydration and wax embedding introduces tissue deformation, in particular the trophoblast shells appear to collapse onto the villi network, creating the false appearance of a double-layered trophoblast shell (Figure S2B,E). Tissue deformation occurred to much less extent with critical point dried specimens (Figure S2C). Whilst, cryo-freezing seems to have preserved the physiological morphology of specimens with intact trophoblast shells and stroma. However, synchrotron micro-CT imaging of cryo-frozen specimens requires a cryo-stream or cold stage to maintain the specimen at cryo-condition during scanning. Figure S1 provides a summary of various sample processing conditions tested here and a flow chart to determine an appropriate processing pipeline.

(ii). Characterisation of feto-placental vascular network in 3D

A cubic sample volume of ≈ 8 mm^3 was scanned, segmented and analysed to identify

bioRxiv preprint doi: https://doi.org/10.1101/2020.12.07.411462; this version posted December 7, 2020. The copyright holder for this preprint (which was not certified by peer review) is the author/funder, who has granted bioRxiv a license to display the preprint in perpetuity. It is made available under aCC-BY 4.0 International license.

placental tissue architecture across multiple scales (Figure 1 and Supplementary Video 1). A disambiguated 3D rendering (Figure 1B) from the entire volume of tissue demonstrates the sample tissue size and three-dimensionality achieved with the technique, while the detail in the terminal capillary loops and surrounding villous tissue (Figure 1G) demonstrate the resolution. Two separate 2D U-Nets (Figure S1) were used alongside expert "ground truth" training data (Figure S3) to fully segment the feto-placental vascular network and the maternal and fetal blood volumes (Figure 1C, E, F, G).

Once the complex tissue had been segmented, multiple data analysis pipelines and simulations could be run, across the imaging scales. Figure 2 displays the skeletonized vascular structure from the entire tissue dataset (2A), a small cropped region (2B) and a single connected tree (2C). The median (interquartile range; IQR) diameter of blood vessels in fixed tissue is 6.8 (6.2 – 8.6) μm for the entire network and 4.4 (IQR: 3.4 - 6.0) μm for a single connected tree (Figure 2D), while the length of blood vessels is 73.8 (IQR: 47.4 - 115.6) μm for the entire network and 21.2 (IQR: 13.6 - 34.1) μm for a single connected tree (Figure 2E). Tortuosity of the blood vessels is 1.2 (IQR: 1.1 - 1.4) for the entire network (Figure S4) and 1.2 (IQR: 1.1 - 1.3) for a single connected tree. A limitation in the current analysis is that skeletonization and quantification of blood vessels for the entire network (Figure 2A) was carried out on down-sampled image data due to computational limitations. Therefore, the measurements from the entire vascular network are likely to be less accurate in comparison to those from the single connected tree, where the full resolution data was used.

B. Characterisation of the porous materno-placental tissue domain in 3D

To characterize the maternal blood porous space, the centre region of the scan ≈ 1.8 mm^3 from the entire data set (see supplementary Figure S3A) and the porous space that encompasses the single connected tree (from Figure 2C) were used. The median (interquartile range; IQR) diameter of pores is 72.2 (50.6 - 97.2) μm for the central region and 57.6 (IQR: 40.6 - 77.8) μm for the single tree region. The diameter of the throat is 27.0 (IQR: 14.4 - 43.6) μm for the central region and 31.0 (IQR: 16.8 - 47.0) μm for the single tree region. The distributions of diameter of porous regions and connecting throats of both the

bioRxiv preprint doi: https://doi.org/10.1101/2020.12.07.411462; this version posted December 7, 2020. The copyright holder for this preprint (which was not certified by peer review) is the author/funder, who has granted bioRxiv a license to display the preprint in perpetuity. It is made available under aCC-BY 4.0 International license.

central region and the region that surrounds the single connected tree (both from specimen 1) are shown in Figure 2H and 2I.

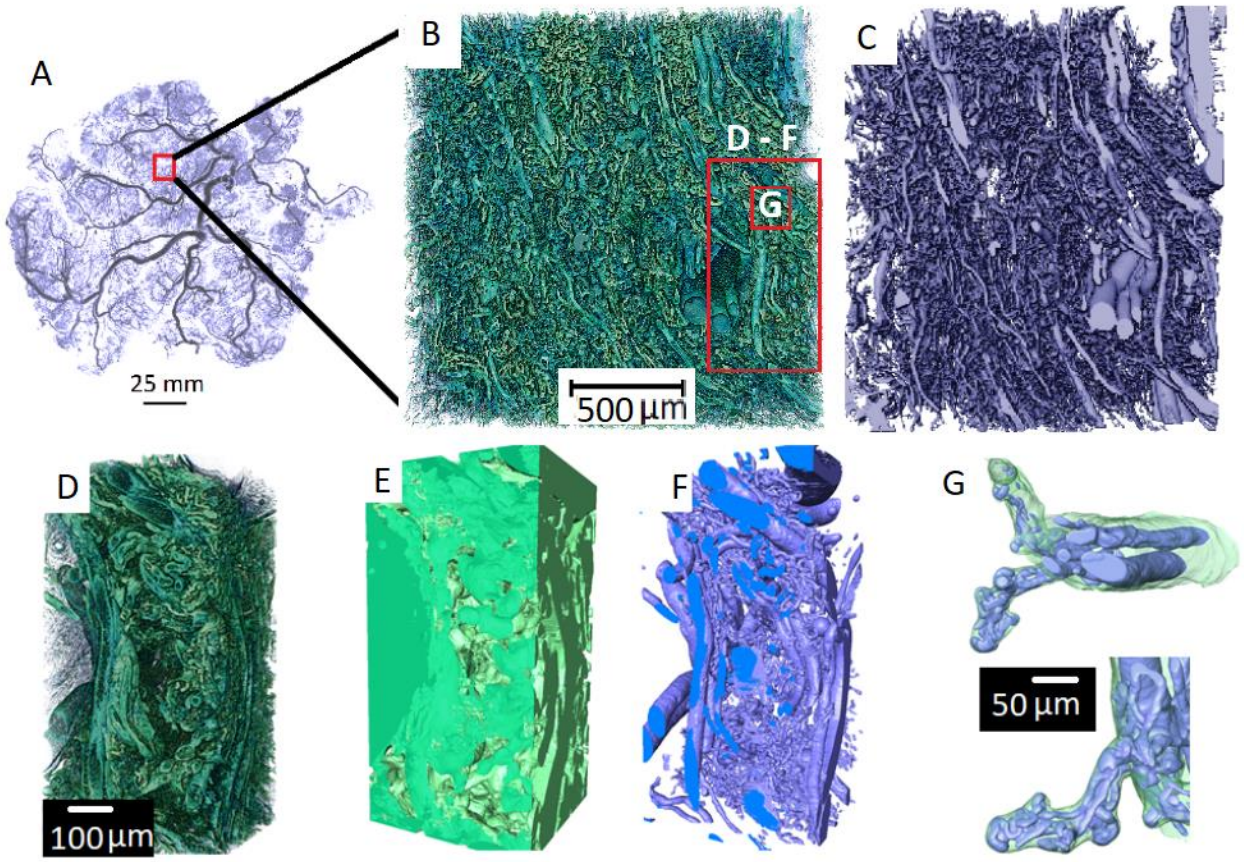

FIG. 1: Multi-scale tissue architecture of placental tissue from synchrotron micro-CT. (**A**) Placental cast under micro-CT [unpublished image from (*5*)]. (**B-G**) Images demonstrating the complex hierarchical architecture of the human placenta (Specimen 1). (**B**) 3D rendering of ≈ 8 mm^3 human placental tissue. (**C**) Fetal vascular network segmented from placental tissue using a U-Net algorithm. (**D-F**) A small section of the placental tissue was cropped from the original dataset (red box in *B*) and 3D rendered. (**D**) 3D rendering of ≈ 0.2 mm^3 tissue showing different hierarchical features. (**E**) U-Net segmented fetal tissue component, (**F**) fetal vessels and (**G**) fetal capillary network with surrounding villous tissue overlaid.

The median and interquartile ranges of diameter of pore and throat, length of throat and

bioRxiv preprint doi: https://doi.org/10.1101/2020.12.07.411462; this version posted December 7, 2020. The copyright holder for this preprint (which was not certified by peer review) is the author/funder, who has granted bioRxiv a license to display the preprint in perpetuity. It is made available under aCC-BY 4.0 International license.

number of connected pores were also analysed for both Specimens 1 and 2, and the results are presented in supplementary Figure S5. These analyses were performed on central tissue regions only.

The flow tortuosity of porous regions was plotted with different minimal lengths. The smallest minimal length employed here (85 μm) is bigger than the mean diameter of a pore (≈ 80 μm) since the blood flow inside a single pore is considered straight. Supplementary Figure S6G shows that the porous tortuosity falls between 1 and 3 in both Specimen 1 and 2.

C. Mesoscopic flow analysis in the human placenta

The maternal flow velocity in the intervillous space was simulated for a fixed pressure gradient applied in three principal directions (Figure 3 and Supplementary Video 2). The relationship between fetal tissue (Figure 3A(i)) and maternal flow (Figure 3A(ii)) in velocity map and streamlines respectively and the inter-relationship between maternal flow streamlines (Figure 3B) and fetal vascular network (Figure 3C) were visualized. The distribution of flow velocities (Figure 3D) were in the range 0 – 1670 (mean: 8) μm/s in the x direction, 0 – 1670 (mean: 10) μm/s in the y direction, and 0 - 1660 (mean: 7) μm/s in the z direction respectively.

Despite the approximately 1:2:1 (x:y:z) aspect ratio of the studied porous domain, the flow resistance in the y direction was found to be approximately twice as small as in the x and z directions, with the corresponding diagonal components of the empirical hydraulic permeability tensor ≈ (1.5, 3.4, 2.0) μm^2, indicating a relatively strong flow anisotropy of the intervillous space.

The connectivity of the intervillous domain was also explored as a function of the minimal pore-throat diameter needed to connect a random central pore to the periphery of the domain (Figure S6A-F). Such critical diameter was found to be just about 25% of the pore size, pointing to a highly connected intervillous space that facilitates flow-limited transport at the tissue mesoscale of ~ 1 mm (see S8 in the Supplementary Text for more details).

bioRxiv preprint doi: https://doi.org/10.1101/2020.12.07.411462; this version posted December 7, 2020. The copyright holder for this preprint (which was not certified by peer review) is the author/funder, who has granted bioRxiv a license to display the preprint in perpetuity. It is made available under aCC-BY 4.0 International license.

D. Uncertainty quantification and scale-dependence of morphological metrics

Placental tissue area fraction fluctuates across the 3D volume in both specimens. Based on the central tissue region (≈ 1.8 mm^3), the area fraction of Specimen 1 ranges from 0.54 to 0.73 (mean: 0.64) and that of Specimen 2 ranges from 0.58 to 0.71 (mean: 0.65; see Figure 4A and Supplementary Figure S7A, B). The tissue volume fractions for Specimens 1 and 2 are 0.64 and 0.65 respectively. Figure 4B shows how the standard deviation of the volume fraction decreases with increasing ROI size (see also Figure S7C). The scale-dependent error in fetal tissue volume fraction, specific surface area (Figure 4C) and the 2-point correlation function vs. distance for both specimens (Figure 4D) are also presented.

Figure 4C illustrates that the relative magnitude of fluctuations in both the tissue volume fraction and specific surface area fall approximately inversely proportional to the square root of the ROI volume ($\sigma/\mu \sim V_{ROI}^{-1/2}$) for the sufficiently large ROI size (compared to the characteristic lengthscale $\lambda \sim 200$ μm; see Figure 4D and Table 1). This is in agreement with theoretical predictions for a generic porous medium (see S9 in the Supplementary Text for more details). Thus, to reduce the estimation error in morphological metrics by a factor of 2, a four-fold increase in the ROI volume is required. For smaller ROI volumes (i.e. when the ROI size is less than ca. 200 μm), the morphometric fluctuations are even more sensitive to the measurement scale.

Three-dimensional (3D) morphometrics were also compared to the estimates based on two-dimensional (2D) 'virtual' stereology (Figure S8) on the same dataset. Table 1 reports the villous tissue volume fraction and specific surface area for Specimen 2 estimated by traditional 2D stereology and 3D morphological analysis. Comparison to the direct 3D estimates (Table 1) shows good agreement for the volume fraction but an up to 40% relative difference for the specific surface area.

bioRxiv preprint doi: https://doi.org/10.1101/2020.12.07.411462; this version posted December 7, 2020. The copyright holder for this preprint (which was not certified by peer review) is the author/funder, who has granted bioRxiv a license to display the preprint in perpetuity. It is made available under aCC-BY 4.0 International license.

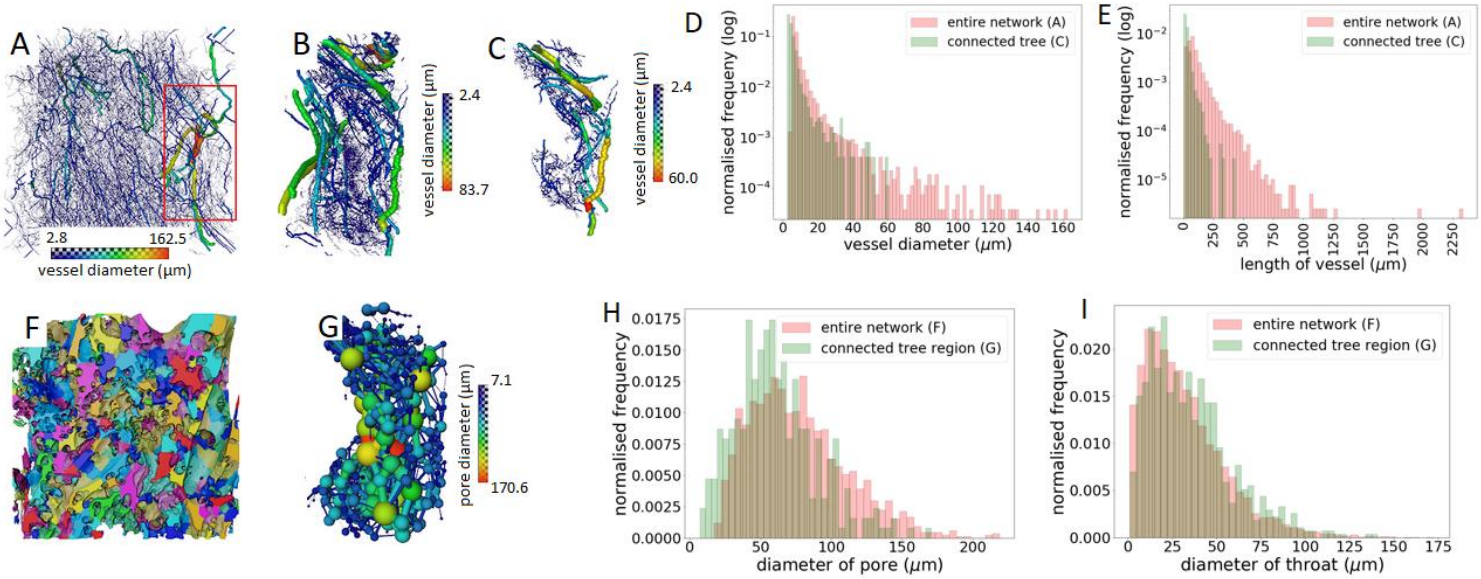

FIG. 2: 3D analysis of the structure of the fetal vascular network and maternal porous space. (**A & B**) Skeletonized vascular structure from the entire tissue volume and from a small cropped region (the red box in *A*). (**C**) shows a single connected vascular tree in the cropped region shown in *B*. (**D & E**) Distributions of vessel diameter and length of blood vessels from the entire fetal vascular network and the connected vascular tree shown in *A* and *c* respectively. (**F**) Porous regions in the central tissue region (≈ 1.8 mm^3). The colors represent different porous regions but are not related to the sizes of the pores. (**G**) Ball and stick model to represent pores and throats in the cropped region as in *C*. (**H & I**) Distributions of diameters of porous regions and connecting throats in the central tissue region and the region that encompasses the single connected tree in *C*.

TABLE 1: Comparison of 2D- and 3D-based placental tissue morphometrics.

Structural metric	2D stereology (mean ± SD)	3D micro-CT
Volume fraction [a]	0.67 ± 0.04	0.65
Slice-averaged area fraction [b]	N/A	0.65 ± 0.03
Specific surface area (S_V, μm^{-1})[c]	0.028 ± 0.006 (range: 0.017 – 0.037)	0.045
Characteristic correlation lengthscale (λ, μm)[d]	N/A	≈ 200

[a] Based on the 2D ROI area of ≈ 1.46 × 1.46 mm^2.
[b] Based on the central ROI volume of ≈ 1.22 × 1.22 × 1.22 mm^3.
[c] Based on the ROI area of ≈ 0.44 × 0.44 mm^2.
[d] The distance at which the mean of normalized auto-correlation function falls below 1%.
N/A indicates the technique is not applicable.

bioRxiv preprint doi: https://doi.org/10.1101/2020.12.07.411462; this version posted December 7, 2020. The copyright holder for this preprint (which was not certified by peer review) is the author/funder, who has granted bioRxiv a license to display the preprint in perpetuity. It is made available under aCC-BY 4.0 International license.

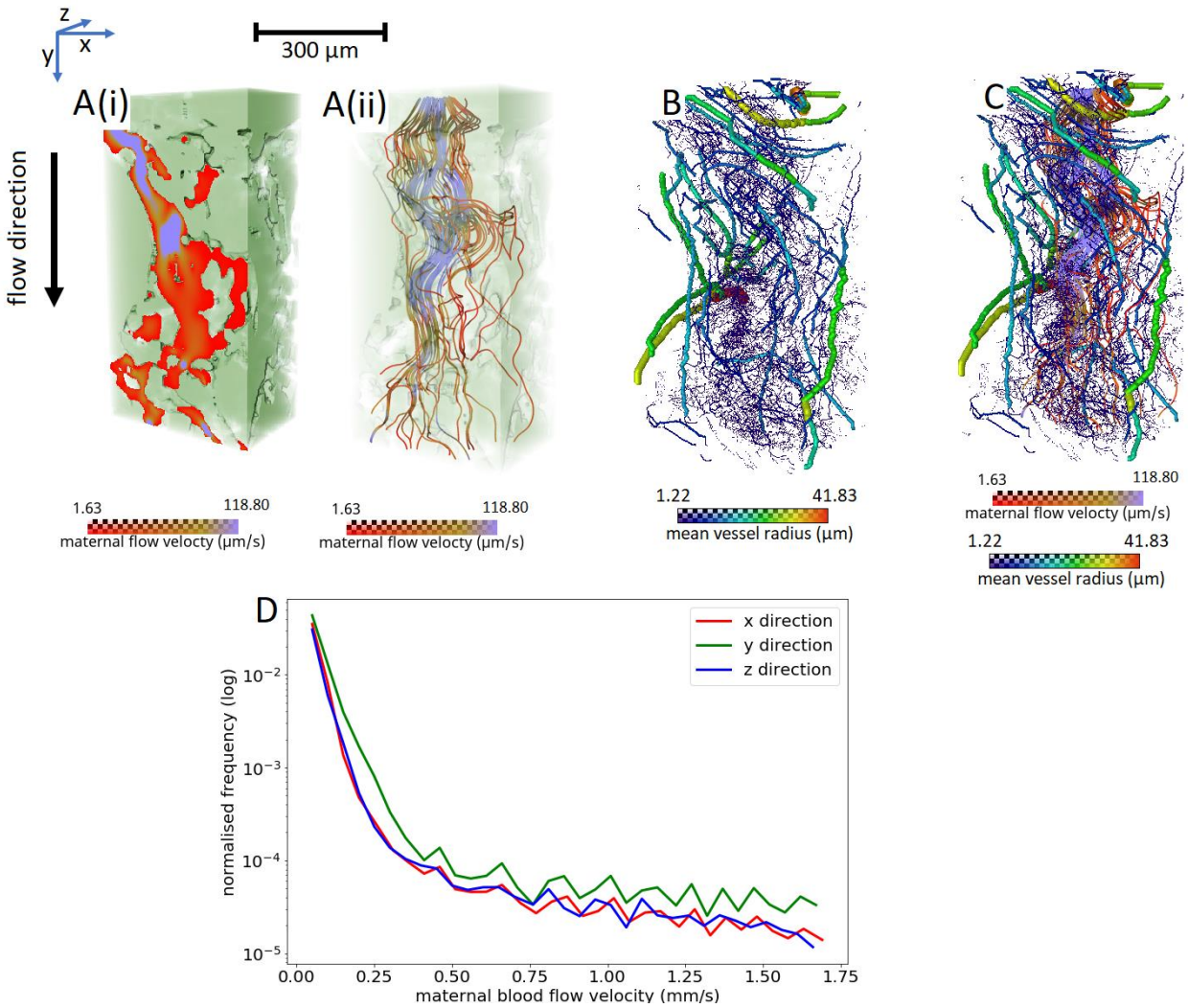

FIG. 3: Flow simulations across maternal intervillous space to visualize the inter-relationship between maternal blood flow and fetal vascular flow. (**A**) shows the maternal (i) flow velocity map and (ii) flow streamlines in the intervillous space. (**B & C**) show the inter-relationship of maternal flow streamlines and fetal blood vascular network. (**D**) Line graphs comparing the maternal blood flow velocity distributions in three different directions with a fixed pressure gradient. x-axis of the graph shows maternal blood flow velocity and y-axis shows the normalised frequency in logarithmic values.

bioRxiv preprint doi: https://doi.org/10.1101/2020.12.07.411462; this version posted December 7, 2020. The copyright holder for this preprint (which was not certified by peer review) is the author/funder, who has granted bioRxiv a license to display the preprint in perpetuity. It is made available under aCC-BY 4.0 International license.

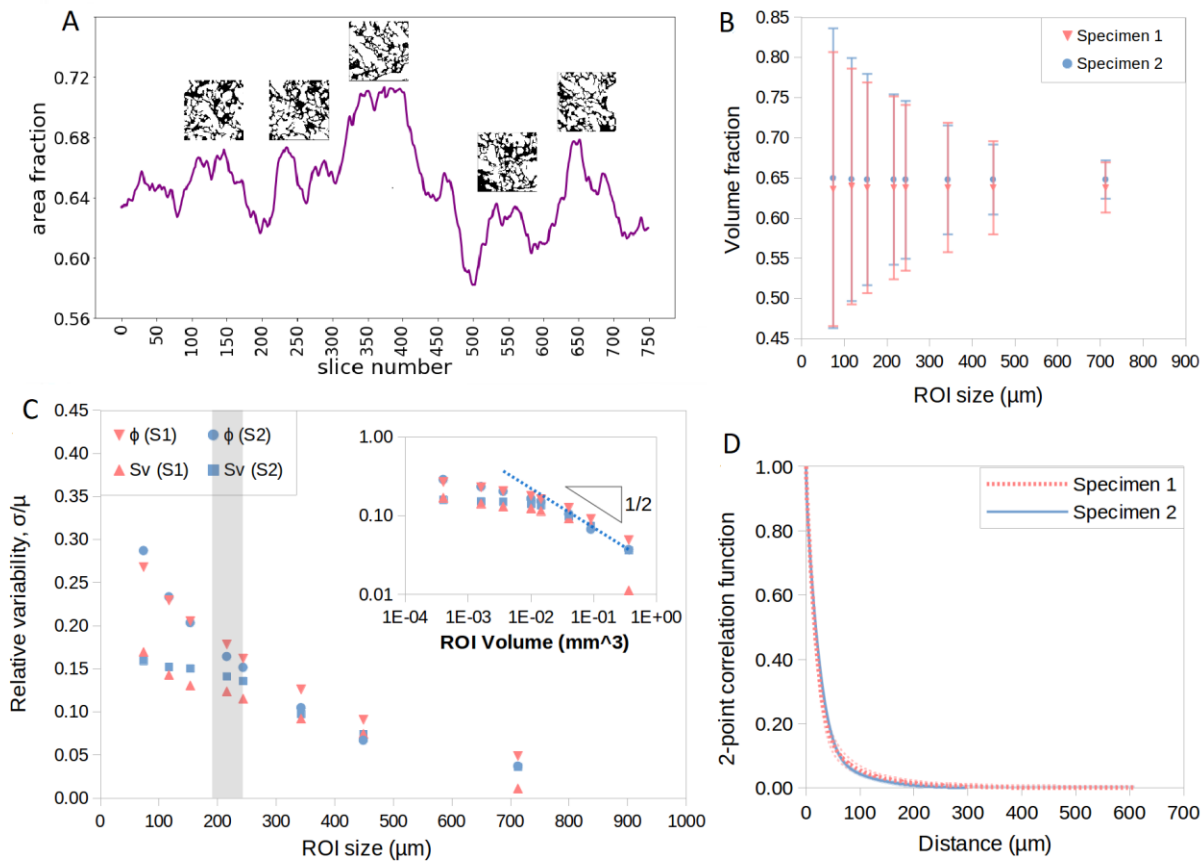

FIG. 4: Uncertainty quantification and scale-dependence of morphological metrics. (**A**) Fluctuations of placental villous tissue area fraction in Specimen 2 for the region of interest (ROI) with the volume of ≈ 1.22 × 1.22 × 1.22 mm^3 (insets illustrate selected slices). (**B**) Volume fraction fluctuations (mean±SD) vs. effective ROI size. (**C**) Scale-dependence of a relative error in the tissue volume fraction (φ) and specific surface area (S_v) estimates; the inset compares to the theoretical prediction of ~ (ROI Volume)$^{1/2}$ on a logarithmic scale. (**D**) Radial two-point autocorrelation function (mean; SD is shown with shaded lines); the corresponding approximate transition range to uncorrelated meso-scale is shown as a grey stripe in *C*.

III. DISCUSSION

In this study, we present a novel approach to quantitatively characterise the 3D structure of complex mesoscale tissues using the human placenta as a model. We demonstrate, how, up to four orders of magnitude can be bridged in a single imaging dataset using synchrotron X-ray micro-tomography; and propose an optimized pipeline for tissue sample processing, contrast reagent perfusion and image segmentation to robustly evaluate the morphological

bioRxiv preprint doi: https://doi.org/10.1101/2020.12.07.411462; this version posted December 7, 2020. The copyright holder for this preprint (which was not certified by peer review) is the author/funder, who has granted bioRxiv a license to display the preprint in perpetuity. It is made available under aCC-BY 4.0 International license.

data of complex vascular systems. To our knowledge, this is the first study to characterise the maternal placental intervillous porous region and to demonstrate the inter-relationship between maternal blood flow and fetal vascular network. Finally, we compare the traditional stereological approaches with direct 3D structural analysis and quantify the scale-dependent fluctuations in common morphological metrics. The developed framework helps to identify a minimal characteristic size for heterogeneous placental and other complex soft tissues and provides the tools to control the associated uncertainties for robust and scalable predictions.

The placental specimens in this study were prepared using different tissue processing techniques (critical point (CP)-drying, fresh-frozen, wax-embedding) and perfused with different contrast agents (Batson's and Yasuaki's; Table S1). CP-dried and wax-embedded specimens showed more deformation and shrinkage of villous tissue in comparison to fresh-frozen specimens that maintained the tissue at near-native anatomical condition. With regards to image data quality, CP-dried specimens displayed the best contrast between fetal tissue and maternal intervillous space among the three processing techniques (Figure S2). Yasuaki's gave a superior contrast of the fetal vascular network than Batson's, meaning Yasuaki's-perfused specimens could be easily segmented with basic contrast-based image segmentation methods while Batson's-perfused specimens would demand a more complex, segmentation strategy. However, one clear drawback with Yasuaki's resin was lower perfusion efficiency which was more evidently observed in smaller arterioles and venules and the terminal capillaries. Figure S1 details the advantages and shortcomings of different sample processing, and demonstrates the most appropriate procedures depending on the region of interest and available segmentation technique(s) for downstream data analysis. In an ideal case, delivered specimen would immediately be Z7 fixed, fetal network infiltrated with a resin, paraformaldehyde (PFA) fixed, and then if a cryo-stage is available then cryo-freeze specimen and micro-CT under cryo-conditions. If a cryo-stage is not available then specimens should be ethanol dehydrated and critical point dried before scanning under ambient condition. In order to segment the various structures a machine-learning algorithm (U-Net) should be employed. This proposed sample preparation and imaging pipeline would be applicable to other vascular-rich organs (*12-14*).

bioRxiv preprint doi: https://doi.org/10.1101/2020.12.07.411462; this version posted December 7, 2020. The copyright holder for this preprint (which was not certified by peer review) is the author/funder, who has granted bioRxiv a license to display the preprint in perpetuity. It is made available under aCC-BY 4.0 International license.

In recent years, automatic or semi-automatic segmentation methods using deep learning algorithms have become popular in the vascular biology (*15*) and placental biology fields (*16*). Convolution neural networks (e.g. U-Net) have been successfully applied in segmenting various vascular systems including retina (*17, 18*) and brain (*19*). Similarly, U-Net has been introduced to placental biologists and used to segment the whole placental volume (*20*). Although the potential usefulness of U-Net in placental vessel segmentation has been shown in a previous study (*21*), only a small number of larger vessels were segmented, and the algorithm applied was relatively primitive. Here for the first time, we apply a U-Net towards multi-domain segmentation of the intricate fetal vascular network and maternal porous space, including terminal capillary loops, where vessel diameters are smaller than 50 μm. The semi-automatic algorithm applied in this study has been used to segment both maternal tissue and the vascular network, and requires a minimal amount of training data in each case (≈ 1% of entire volume). The most striking aspect of the U-Net segmentation is the detection of the smallest terminal capillaries, with diameters of the fixed tissue as small as ≈ 2.5 μm (IQR: 6.2 - 8.6). These tiny terminal capillaries are exceedingly difficult to segment manually, so their presence in the U-Net segmentation provides a less time-consuming and more consistent method for their inclusion in analyses

The reliability of the U-Net predictions was assessed by dice score coefficient, a commonly used voxel-based validation metric for image segmentation algorithms (*22*). Using the dice score, previous comparisons between multiple manual expert segmentations of biological components have varied between ≈ 0.27 and ≈ 0.69 (*23*). When comparing the U-Net segmentations to expert manual validation segmentations, the dice scores for vascular and tissue regions are 0.8 and 0.9 respectively (Figure S9). There are, however, a few artefacts present in the U-Net segmentation (mislabelling of maternal porous region as fetal tissue) that could lead to overestimation of the surface area of fetal tissue. In addition, the current U-Net model was not able to generalize across datasets, instead requiring manual training data from each individual dataset. This may be due to the variation in specimen processing and imaging, which manifested significantly different appearances in the final datasets.

Understanding the structural development of the placenta is critical since the common

bioRxiv preprint doi: https://doi.org/10.1101/2020.12.07.411462; this version posted December 7, 2020. The copyright holder for this preprint (which was not certified by peer review) is the author/funder, who has granted bioRxiv a license to display the preprint in perpetuity. It is made available under aCC-BY 4.0 International license.

pregnancy disorders fetal growth restriction (FGR) and pre-eclampsia are associated with impaired development of the placental vascular network (*24, 25*). The human placenta is hemochorial and possesses a dual blood supply; maternal and fetal circulations are separated, but work collaboratively as a multi-villous exchange system (*26*). Defects in either supply could impair the nutrient and gaseous exchange. Using the above specimen processing and segmentation workflow, we have quantified the continuous fetal vascular networks from a ≈ 8 mm^3 placental tissue block. Our findings show that the tissue block captures a transition from the micro- to meso-scale, with the size range of blood vessels and intervillous pores of the order of 10 to 1000 μm (Figure 2). In order to appreciate the spatial inter-relationship between these two circulations, we have generated the maternal flow intertwined with the fetal vascular network (Figure 3C). We simulated maternal blood flow in a large portion of the segmented intervillous pore space for a fixed pressure gradient of ~ 10 Pa/mm within placental tissue (*27, 28*). The predicted flow had an exponential distribution of velocities, typical for a random porous medium (*29*), with the range of ≈ 0 – 2 mm/s. This is consistent with previous MRI *in vivo* estimations that reported regions of slow (< 0.5 mm/s) and fast (> 1 mm/s) blood flow (*30*). Furthermore, our results suggest a new hypothesis that local IVS pore sizes influence nutrient and gaseous exchange efficacy. Specifically, further studies might aim to study whether IVS porosity spatially correlates with the calibres and orientation of associated villous microvessels, to determine maternal-fetal placental flow matching efficacy.

With the intention of understanding the normal physiological blood flow and deviations occurring in diseased pregnancies, numerous mathematical and computational models have been developed and attempt to replicate the utero-placental circulations (*11, 31-33*). A particular challenge is the geometric complexity of intervillous maternal porous regions which are difficult to characterize (*32*); therefore, there is a lack of knowledge on placental porous structure. Porosity within human tissues has been extensively investigated in bone and other soft tissues (e.g. adipose tissue) from the perspective of tissue engineering (*34-37*). Nonetheless, the placental maternal intervillous space porous medium has been less well studied and reported. In this study, we have quantified the size of porous regions, the connecting throats between individual pores, and the length of connecting throats.

bioRxiv preprint doi: https://doi.org/10.1101/2020.12.07.411462; this version posted December 7, 2020. The copyright holder for this preprint (which was not certified by peer review) is the author/funder, who has granted bioRxiv a license to display the preprint in perpetuity. It is made available under aCC-BY 4.0 International license.

Moreover, we report the number of coordination for individual pores, and also visually examine the connectivity by thresholding the size of connected regions (Figure S6). Both qualitative and quantitative analyses suggest that the maternal porous space is highly connected and there is no unconnected, isolated porous region. The minimal diameter of throat is 0.86 μm (IQR: 14.4 - 43.6), in line with the average thickness of a human red blood cell (0.8 - 1 μm), indicating blood flow could occur throughout the porous medium with some impedance (*38*). However, the resistance to IVS flow would vary depending on the length and diameter of connecting throats/pores, suggesting a potential explanation for the heterogeneous maternal flow velocity reported in (*28*) and also in our flow simulations.

Contrast imaging and mesoscopic flow analysis reported here for the placenta could readily be applied to other organs where there is a challenge to understand structure function relationships when a fluid circulates around epithelia or where flow is not confined to a vascularised system. Examples of this anatomy type are in the intestine and the central canal of the spine, in similarity with the placenta. In the gut, uptake of nutrients and therapeutic compounds occur from the crypts of the jejunum lumen, passing into the systemic circulation having traversed associated villi. The crypt lumen has been observed to become vacuolated following chemotherapy, altering their porosity, which is hypothesised to effect the efficacy of nutrient and therapeutic uptake (*39*). In a second example, the motile cilia of the spinal cord central column and brain generate an efficiency of cerebrospinal fluid flow that is sensed and regulates structural modelling of the shape of an organism during embryonic development (*40*). As a final example, draining lymph nodes swell in response to infection to increase lymphocytes and thereby increasing the likelihood of meeting antigens to boost immune response. Lymph node enlargement coincides with intranodal lymphangiogenesis, enlarged lymphatic sinus and medullary regions all of which participate in fluid transport and exchange (*41*). Thus, the workflow we have developed could provide anatomical insights on tissue in homeostasis and pathology.

Another important point to note here is that pore diameters could be influenced by the flow and the hydrostatic pressure within the intervillous space (IVS) during perfusion/fixing. Quite often when placental tissue is fixed for morphological analysis and stereology, it is

bioRxiv preprint doi: https://doi.org/10.1101/2020.12.07.411462; this version posted December 7, 2020. The copyright holder for this preprint (which was not certified by peer review) is the author/funder, who has granted bioRxiv a license to display the preprint in perpetuity. It is made available under aCC-BY 4.0 International license.

done so under static conditions of flow (*42*). Following partum, the placenta collapses and loses a significant volume of maternal blood from the intervillous space. Hydrostatic pressure from flow within the IVS *in vivo* can be recapitulated during *ex vivo* dual perfusion of the human placenta, yielding a more normal spatial arrangement of villi compared to the arrangement produced by the direct immersion fixing of deflated placental material. Consequently, most historic stereological analyses have likely under-estimated the volume densities of the IVS in this tissue (*42*). In turn this will have led to an under-representation of pore size diameter and connectivity characteristics.

One unresolved question is how to determine the tissue sample size required to accurately obtain representative and statistically-precise data. This is particularly true for placental tissue due to its inherent heterogeneous nature. While it is true that the larger the tissue section, the more information one can retrieve, using a large-sized sample comes with technical and economic burdens. Therefore, systematically characterising the minimal tissue size that could provide adequate information with the least error would be advantageous. Using uncertainty quantification and the scale-dependence of morphological metrics applied to a variety of placental tissue samples, we identified a transition from microscopic fluctuations to tissue-scale properties at the mesoscale of ~ 200 μm (Table 1). Thus, the smallest ROI volume required, without failing to comprehend the heterogeneous nature of the finest features of exchange villi (e.g. terminal villi) in placental tissue, is of the order of magnitude of 0.1 mm^3 (see Figure 4). Although, this smallest cut-off point might vary in other tissues with different geometric properties (e.g. larger blood vessels), the generic scale-dependence of the magnitude of 3D morphometric fluctuations (inversely proportional to the square root of the ROI volume) is shown to be sufficiently universal for a wide class of porous media found in biological solute and gas exchangers. Future work is needed to further refine and extend the developed framework in placental pathologies and to other organs.

In conclusion, this paper offers both a novel approach and a validated workflow for massively multi-scale characterization of soft tissues with complex vascular networks. In addition, several detailed morphology and functional characteristics of our chosen model

bioRxiv preprint doi: https://doi.org/10.1101/2020.12.07.411462; this version posted December 7, 2020. The copyright holder for this preprint (which was not certified by peer review) is the author/funder, who has granted bioRxiv a license to display the preprint in perpetuity. It is made available under aCC-BY 4.0 International license.

tissue, placenta, have been analysed in 3D. In future, these methods could be applied to placental samples from normal and FGR pregnancies to explore underlying causes of disease and inform potential future treatments.

The new approach was enabled by a combination of innovative sample preparation, advanced synchrotron-based imaging and state-of-the-art segmentation algorithms that allowed to bridge the gap of previously disconnected characterisation by traditional X-ray tomography and angiography (cf. Figure 1A), light microscopy (cf. Figure 1B) and confocal or electron-microscopy (cf. Figure 1F). In the placental research arena the data generated here represents a first. While, the recommendations provided for future researchers should allow imitating the workflow to quantify structures in other tissues such as bone marrow, kidney and lungs.

IV. METHODS

A. Specimen collection and preparation

1. *Ex vivo* placental perfusion and preparation of tissue blocks

Ex vivo dual perfusion of human placental cotyledons was conducted as previously described (*42*) from two pregnancies complicated by fetal growth restriction (FGR) and two from uncomplicated pregnancies (Table S1). Briefly, placentas were collected within 30 minutes of delivery and the chorionic plate artery and vein corresponding to an intact cotyledon were each cannulated. Fetal-side perfusion was commenced in an open circuit at 6 mL/min with a modified Earle's bicarbonate buffer, gassed with 5% CO_2 / bal. N_2. Following a quality control check at T=5 minutes that fetal-side venous outflow was ≥ 75% of fetal-side inflow, the maternal-side perfusion was commenced in open circuit at 14 mL/min with the same buffer, gassed with 21% O_2 / 5% CO_2 / bal. N_2, via a single glass cannula (i.d. = 2 mm) held 5 mm below the decidua surface. The cotyledons continued to be perfused in open circuit for three hours prior to perfusion fixation from the maternal surface with Zinc 7 fixative Lykidis, 2007 for 15 minutes. Various contrast reagents were infused into the fetal or maternal circulatory compartments (Table S1).

bioRxiv preprint doi: https://doi.org/10.1101/2020.12.07.411462; this version posted December 7, 2020. The copyright holder for this preprint (which was not certified by peer review) is the author/funder, who has granted bioRxiv a license to display the preprint in perpetuity. It is made available under aCC-BY 4.0 International license.

LDH-based (Yasuaki) contrasting resin: Colloidal dispersion of NiAl layered double hydroxide (LDH) was prepared following our previous report (*43*). Briefly, $NiCl_2 \cdot 6H_2O$ and $AlCl_3 \cdot 6H_2O$ were dissolved in a mixture of EtOH and ultra-pure water followed by the addition of acetylacetone (acac). To this mixture, propylene oxide (PO) was added as an alkalization agent (*44*) and the container was sealed and kept at a room temperature (~ 20°C). The obtained suspension was kept in a freezer (−20°C) and then dried under a vacuumed condition (<10 Pa), yielding dried NiAl LDH nanoparticles. To make up 5 mL of resin, the powdery NiAl LDH (1.0 g) was dispersed in ethanol (EtOH; 2.5 mL), and then methyltriethoxysilane (MTES; 2.0 mL) and tetraethyl orthosilicate (TEOS; 0.5 mL) were added to this mixture. Then, H_2O (0.7 mL) was added just before perfusion to initiate the gelation reaction. The procedures were performed under stirring at a room temperature. This resin was applied immediately after fixing the lobule *in situ* within the perfusion cabinet, ahead of any other contrast reagents that might have been used.

Batson's resin contrast: On occasions a Batson's resin from the "Batson's no. 17 Anatomical Corrosion Kit" (Polysciences, Inc., Europe) was applied to the fetal circulation following perfusion. The liquid resin was prepared as a 20 mL base solution, 2.4 mL of catalyst and one drop of promoter; and manually injected via the chorionic plate arterial cannula until emergent at the chorionic plate vein cannula. Both cannulae were clamped and the whole lobule was allowed to polymerise overnight on iced water, within a sealed plastic bag.

Tissue processing: The postperfusion fixed and post-contrast-infused cotyledon was excised from the non-perfused tissue and a 5 mm vertical slice of the cotyledon, adjacent to the inflow locus of the maternal cannula, was dissected from the cotyledon and fixed in a PFA fixative overnight to stiffen and further preserve the tissue. In all cases, following PFA diffusion fixing, 5 mm sized cubes were dissected from the vertical tissue sections and stored in sterile PBS. In some cases, the small blocks were infused with a further contrast agent, phosphotungstic acid (PTA), for several days or hours. In other cases, the cubes underwent critical point drying using an E3100 Critical Point Dryer (Quorum, UK), following manufacturer's instructions, and dipped into liquid nitrogen to freeze fracture a 3 x 3 mm^2 cross-sectional sample for imaging, or prior to wax embedding.

The methods for processing whole-organ vascular casts (see Figure 1A) were as previously

bioRxiv preprint doi: https://doi.org/10.1101/2020.12.07.411462; this version posted December 7, 2020. The copyright holder for this preprint (which was not certified by peer review) is the author/funder, who has granted bioRxiv a license to display the preprint in perpetuity. It is made available under aCC-BY 4.0 International license.

described (*5*).

2. 3D tomographic imaging

At the Diamond Light Source (DLS) facility (Harwell, UK; Manchester Imaging Branchline, I13-2), in-line high-resolution synchrotron-sourced phase contrast micro-computed X-ray tomography was used to generate images, following various methodologies to optimise image quality and feature extraction (*45, 46*). Briefly, micro-computed tomography employed filtered (1.3 mm pyrolytic graphite and 3.2 mm Al filters) polychromatic X-ray beams with energy in the range of 8−30 keV were used to probe the samples. Transmitted X-rays produce visible light on striking a scintillator (500 μm thick CdWO4) positioned between 60 to 100 mm away in-line with the sample. The light was then magnified with various objectives and imaged on a sCMOS (2560 x 2160 px) detector (pco.edge 5.5; PCO AG, Germany). Optical magnification of 8x was employed resulting in an effective isotropic px size of 0.81 μm. In total, 3001 – 4001 X-ray projections were recorded over 0 – 180° rotation at using exposure time between 80 to 200 ms. Projections were reconstructed into 3D datasets using a filtered-back projection algorithm (*47*) incorporating dark- and flat-field correction, ring artefact suppression and lens-blurring (*48, 49*).

Samples were prepared following various methodologies (see more details above and in Table S1) to optimise image quality and feature extraction. One critical point-dried air-filled sample (3 × 3 mm^2 cross-section) was scanned at room temperature (Specimen 1; 60 mm S-D distance, 3001 projections, 0.08 s exposure). Another sample (3 × 3 × 3 mm^3) was plunge frozen into liquid nitrogen and scanned (Specimen 2; 60 mm S-D distance, 4001 projections, 0.15 s exposures) whilst maintaining a sample temperature of −20℃ using a cold stage (*50*). The third dehydrated and wax-embedded sample (3 × 3 × 3 mm^3 cubed section) was scanned at room temperature (Specimen 3; 100 mm S-D distance, 4001 projections, 0.2 s exposure). See Table S1 for more details.

B. Segmentation

To segment the mesoscopic features from Specimen 1, creation of 'ground-truth' training

bioRxiv preprint doi: https://doi.org/10.1101/2020.12.07.411462; this version posted December 7, 2020. The copyright holder for this preprint (which was not certified by peer review) is the author/funder, who has granted bioRxiv a license to display the preprint in perpetuity. It is made available under aCC-BY 4.0 International license.

data was accomplished using SuRVoS (Super Region Volume Segmentation Workbench) which applies a supervoxel segmentation strategy as described in (*51*). A 256 × 256 × 256 px (0.21 x 0.21 x 0.21 mm) region of the full resolution volume was segmented for the feto-placental vascular network and a 384 × 384 × 384 px (0.31 x 0.31 x 0.31 mm) region was segmented into the maternal and fetal blood volumes. These segmented regions along with the corresponding image data were then used to train two separate 2D U-Net deep learning models for binary segmentation (*52*). All aspects of model construction, training and data prediction were done using the fastai deep learning Python library (*53*). The U-Net model architecture used a ResNet34 (*54*) encoder that accepts images of size 256 × 256 px and that had been pre-trained on the ImageNet dataset (*55*). For model training, both the segmented label volumes and the corresponding data volumes were sliced into 2-dimensional images parallel to the xy, xz and yz planes. For each model, a randomised dataset was created from the pool of images with an 80%/20% split between training and validation image sets. The default fastai image transformations and augmentations were used. Model training was carried out using binary cross-entropy as the loss function and evaluated using the Intersection over Union (IoU/Jaccard) score as the metric on the validation set. For the vascular network data, training was carried out for 10 epochs giving a final IoU score of 0.93 on the validation set, the loss for the training set was 0.056 and the corresponding loss for the validation set was 0.052. For the maternal/fetal blood volumes, training was carried out for 15 epochs, giving a final IoU score of 0.93 on the validation set, the loss for the training set was 0.099 and the corresponding loss for the validation set was 0.097.

To overcome the issues of using a 2-dimensional network to predict 3-dimensional segmentation, a data-averaging approach was developed. To generate the vascular network and maternal/fetal blood volume segmentations for the full 2520 × 2520 × 2120 px (2.05 x 2.05 x 1.72 mm) data, the image data volume was sliced into three stacks of 2-dimensional images parallel to the xy, xz and yz planes. The corresponding segmentation for each of these image stacks was predicted before being recombined back into a 3-dimensional dataset, thereby producing 3 separate segmented volumes. The image data volume was then rotated by 90 degrees around the 4-fold symmetry axis running perpendicular to the xy plane and the entire slicing and prediction process was repeated again. After 4 cycles of this process,

bioRxiv preprint doi: https://doi.org/10.1101/2020.12.07.411462; this version posted December 7, 2020. The copyright holder for this preprint (which was not certified by peer review) is the author/funder, who has granted bioRxiv a license to display the preprint in perpetuity. It is made available under aCC-BY 4.0 International license.

the resulting 12 segmented volumes were summed and a final segmentation produced by applying a threshold to the data where there was agreement between 6 and more or the predictions in the case of the maternal/fetal blood volumes and between 9 and more of the predictions in the case of the blood vessels.

To segment the fetal tissue components from Specimen 2, the central region of the full resolution dataset (2520 x 2520 x 2120 px = 2.05 x 2.05 x 1.72 mm) was cropped to obtain a volume of 1500 x 1500 x 1500 px (1.22 x 1.22 x 1.22 mm) (see Supplementary Figure S3A), which was then down-sampled to obtain a volume of 750 x 750 x 750 px. This down-sampled, cropped, volume was then split into eight sub-volumes, each of which were manually segmented using SuRVoS (Supplementary Figure S3B to S3D).

C. Validation of semi-automated segmentation by U-Net

To validate the U-Net prediction of fetal vascular network in Specimen 1, two different regions of 384 x 384 x 384 px (0.31 x 0.31 x 0.31 mm), which were located away from the original training data, were randomly chosen and SuRVoS-segmented manually. The similarities between the SuRVoS-segmentations and the U-Net predictions (Supplementary Figure S9A and S9B) were compared using the Sørensen–Dice score = $2|M \cap U|/(|M| + |U|)$, which compares the area of the overlap ($M \cap U$) to the average area of the manually-segmented (M) and U-Net-predicted (U) regions respectively (estimated for each slice).

To validate the U-Net prediction of the fetal tissue component in Specimen 1, a similar strategy was used. Dice scores were again calculated between two SuRVoS-segmented Validation Regions (256 x 256 x 256 px = 0.21 x 0.21 x 0.21 mm) and the U-Net prediction (Supplementary Figure S9C and S9D). The fetal tissue area fraction of individual slices was also compared between U-Net predictions and SuRVoS segmentations.

Supplementary Figure S9E and S9F show the dice scores for fetal vascular network segmentation and fetal tissue segmentation respectively. The mean dice score for vascular validation Region #1 is 0.81 and that for vascular validation Region #2 is 0.88. Vascular region #2 is likely to have a higher dice score because it contains fewer but larger vascular

bioRxiv preprint doi: https://doi.org/10.1101/2020.12.07.411462; this version posted December 7, 2020. The copyright holder for this preprint (which was not certified by peer review) is the author/funder, who has granted bioRxiv a license to display the preprint in perpetuity. It is made available under aCC-BY 4.0 International license.

branches in comparison to vascular Region #1. The mean dice scores for tissue validation Region #1 and Region #2 are 0.97 and 0.96 respectively. A higher dice score in the tissue regions as opposed to the vascular regions is expected. This is because the vascular network segmentation has more boundaries than the tissue segmentation where most discrepancies between U-Net and SuRVoS segmentation occur. The area fraction comparison for tissue validation Region #1 and Region #2 (Supplementary Figure S9G) confirms the consistent agreement between U-Net prediction and SuRVoS segmentation.

D. CT-based stereology

Following synchrotron imaging of a placental block, capturing 2520 × 2520 × 2120 px^3 tissue (approximately 8 mm^3) at ≈ 80 μm slice intervals with an image resolution of 0.8125 μm/px, systematic analysis of villous volume density and syncytiotrophoblast surface density was performed using a traditional stereology method, as described previously (*56, 57*). Every 100th image taken was imported into Image J software (*58*), providing 22 images in total (Figure S8A).

Villous volume density estimation: Within each image, a smaller 1800 × 1800 px^2 field of view (FOV) was generated systematically (Figure S8B). A grid of 11 x 11 dots was superimposed on the FOV. The number of grid points hitting the villi and intervillous space was scored and the volume density of each of these morphological features was assessed using

$$V = P_p/P_n ,$$

where V_V is the volume fraction of the feature of interest, P_p is the number of points that hit features of interest, and P_n is the total number of test points in the grid (*57*).

Syncytiotrophoblast surface density estimation: From each synchrotron image, a smaller 543 × 543 px^2 field of view (FOV) was generated systematically as depicted in Figure S8C. A grid of 10 x 10 crosses (line length: 12 μm) was superimposed onto the FOV. In processing for surface density estimation, line intersects with the syncytiotrophoblast were scored (N =

bioRxiv preprint doi: https://doi.org/10.1101/2020.12.07.411462; this version posted December 7, 2020. The copyright holder for this preprint (which was not certified by peer review) is the author/funder, who has granted bioRxiv a license to display the preprint in perpetuity. It is made available under aCC-BY 4.0 International license.

100 intersects per image, N = 22 images). The horizontal lines were used as intercepts to estimate the specific surface area of syncytiotrophoblast $S_{V\,(syn)}$ within tested volume:

$$S_{V\,(syn)} = 2I_L,$$

where I_L is the intersection count fraction (the number of intersections with the villous boundary per unit length of test line) (*59*).

E. 3D morphological analysis

1. Structural analysis of fetal vascular network

The structure of the fetal vascular network (Specimen 1) was analysed using Avizo software 2020.1 (Thermo Fisher Scientific). Using the *'Centreline tree'* module which extracts the center lines of labelled 3D image volume as described in (*60*), the vascular network was skeletonized from placental tissue from the entire dataset of ≈ 8 mm^3 (Figure 2A) and a small cropped region of ≈ 0.2 mm^3 (Figure 2B). The vascular branching structure (length, diameter and tortuosity) of the entire network and a single connected tree inside the small cropped region was analysed. Only the vessels with the diameter greater than or equal to 3 px (2.4 μm) were included since the vessels smaller than that could not be resolved.

2. Maternal porous region analysis

To evaluate the size and connectivity of the porous region (maternal intervillous space), the *'Separate objects'* module (Avizo 2020.1) that uses the watershed method (*61, 62*) was employed on the labelled 3D image volume to separate the porous regions (Figure 2F). Afterwards, the *'Pore Network Model'* module (Avizo) (*60-62*) was applied to generate the spheres at separated porous regions. The centre of two spheres were connected by 'throat' (a throat is a region that connects two individual pores) (Figure 2G).

In analysing the maternal porous region, the central placental tissue region of ≈ 1.8 mm^3 (see supplementary Figure S3A) and the porous region that encompasses the single connected tree (from Figure 2C) were used. Distributions of diameters of pores and throat, length of throat and number of pore coordination (how many pores are connected to an individual

bioRxiv preprint doi: https://doi.org/10.1101/2020.12.07.411462; this version posted December 7, 2020. The copyright holder for this preprint (which was not certified by peer review) is the author/funder, who has granted bioRxiv a license to display the preprint in perpetuity. It is made available under aCC-BY 4.0 International license.

pore) were analysed to characterize the placental porous medium.

The tortuosity of porous regions was analysed using the *'Flow tortuosity'* module (Avizo) which computes the tortuosity based on the flow velocity vector field (the output of the *'Absolute Permeability Experiment Simulation'* module (*60, 61*)). The flow velocity vector was calculated using a fixed pressure drop across the domain (see Section 3 below for more details). Porous tortuosity was computed with various minimal lengths and compared between Specimen 1 and 2.

3. Simulations of maternal blood flow into the intervillous space

Maternal blood flow into the intervillous space was simulated using the *'Absolute permeability experiment simulation'* module (Avizo 2020.1) which solves Stokes flow in a segmented intervillous porous space geometry (*60, 61*). The simulation was performed on the small cropped region of ≈ 0.2 mm^3 (as described above). However, the dataset was downsampled (2 x) as flow simulation on full resolution data would be computationally prohibitive. The simulations were done in three directions (x, y and z) across the tissue thickness of ≈ 500 μm (x and z directions) and ≈ 950 μm (y direction). Three simulations were performed with a fixed pressure gradient across three principal directions (setting the pressure drop of 10 Pa, in the y, or 5 Pa, in the x and z directions respectively, accounting for ≈ 1:2:1 (x:y:z) aspect ratio; i.e. ≈ 10 Pa/mm within tissue (*27, 28*)). The other four domain boundaries (in the transverse to the applied gradient direction) were assumed impermeable in each simulation, and a no-slip flow condition was used at the fluid-solid interfaces. A constant blood viscosity of 0.003 Pa.s was assumed. The calculated net flow rate was used to estimate the empirical hydraulic permeability in each principal direction from Darcy's law (*60*).

4. Characterisation of fetal tissue component

The area and volume fraction of segmented fetal tissue components from Specimen 1 and 2 were analysed using the *'Volume fraction'* (Avizo 2020.1). The surface area of segmented fetal tissue components was analysed using the *'Label analysis'* module (Avizo) which

bioRxiv preprint doi: https://doi.org/10.1101/2020.12.07.411462; this version posted December 7, 2020. The copyright holder for this preprint (which was not certified by peer review) is the author/funder, who has granted bioRxiv a license to display the preprint in perpetuity. It is made available under aCC-BY 4.0 International license.

calculates the surface area of labelled regions from 3D image volume. The area fraction was analysed for individual slices. Volume fraction and surface area were analysed using different region of interest (ROI) sizes. To obtain the ROI cubes at different sizes, the tissue cubes with various x and y length and fixed z thickness (243.75 μm) were cropped without overlapping. For those ROI sizes with more than 1000 ROI cubes, a systematic random sampling method (picking up n^{th} ROI cubes) was used in order to get 1000 random ROI cubes for statistical analysis. For those ROI sizes with fewer than 1000 cubes, all ROI cubes were included. The analysis was done for both Specimen 1 and 2 and performed on the central tissue region (as shown in supplementary Figure S3A).

Statistical Handling

For the purposes of stereology, a systematic random sampling protocol was used, where every 100th image from a stack of 2120 images was analysed for volume fraction and specific surface area (N=22 fields of view).

ACKNOWLEDGMENTS

This work was partially supported by the MRC (MR/N011538/1), EPSRC (EP/T008725/1), Welcome Trust (212980/Z/18/Z) research grants. G.P. would like to acknowledge the EPSRC grant EP/M023877/1 and Great Britain Sasakawa Foundation for funding. The experiment was performed on the Branchline I13-2 of the Diamond Light Source synchrotron in Oxfordshire, UK, on beamtimes MG23941 and MG22562. The authors would like to acknowledge the beamline scientists Dr Andrew Bodey and Dr Shashi Marathe as well as collaborators Dr Saurabh Shah and Prof Peter D. Lee (University College London) for providing access to the cold-stage and assistance with setting up. We also thank Dr James Carr, Dr Tristan Lowe, Dr Kerstin Schirrmann, Ms Ruth Whelan-Jeans and Ms Saskia Port (University of Manchester) for their help with pre-synchrotron optimisation of micro-CT protocols and image analysis at the early stages of this study.

bioRxiv preprint doi: https://doi.org/10.1101/2020.12.07.411462; this version posted December 7, 2020. The copyright holder for this preprint (which was not certified by peer review) is the author/funder, who has granted bioRxiv a license to display the preprint in perpetuity. It is made available under aCC-BY 4.0 International license.

Author Contributions

Win M. Tun performed 3D image data segmentation, data analysis and simulations, created movies and wrote the manuscript.

Gowsihan Poologasundarampillai contributed to project design, performed data collection and data analysis, proposed optimised pipeline for specimen preparation and data segmentation and wrote the manuscript.

Gareth Nye and Helen Bischof refined and performed the perfusion and specimen collection, processed tissue and prepared blocks for synchrotron imaging as well as stereological analysis.

Oliver N. F. King developed the U-Net image segmentation algorithm and wrote the manuscript.

Mark Basham supervised development of U-Net segmentation algorithm, image data segmentation, data analysis and movie creation.

Yasuaki Tokudome developed and manufactured the Yasuaki's resin.

Rohan M. Lewis contributed to the interpretation of the results and provided critical feedback and helped shape the research and wrote the manuscript.

Edward D. Johnstone contributed to the interpretation of the results and provided critical feedback and helped shape the research and wrote the manuscript.

Paul Brownbill conceived and designed the project idea, performed tissue sample collections, sample preparations and stereological analysis, contributed to the interpretation of the results, provided critical feedback, supervised the project and wrote the manuscript.

Michele Darrow supervised image data segmentation and data analysis and simulations, contributed to the interpretation of the results, provided critical feedback, supervised the project and wrote the manuscript.

Igor L. Chernyavsky conceived and designed the project idea, designed and performed the scale dependence error analysis, designed and supervised all findings of this work, supervised the project and wrote the manuscript.

All authors discussed the results and contributed to the writing of the manuscript.

bioRxiv preprint doi: https://doi.org/10.1101/2020.12.07.411462; this version posted December 7, 2020. The copyright holder for this preprint (which was not certified by peer review) is the author/funder, who has granted bioRxiv a license to display the preprint in perpetuity. It is made available under aCC-BY 4.0 International license.

Competing Interests

The authors declare no competing interests.

Data availability

All data needed to evaluate the results and conclusions are present in the paper and/or the Supplementary Materials. The reconstructed micro-CT volumes (DLS ID 120077 and 13761), manual segmentations (DLS ID 120077) and the training data for U-net and predicted final segmentations (DLS ID 123861) will be released on public repository EMPIAR (https://www.ebi.ac.uk/pdbe/emdb/empiar/). The trained U-net models for segmenting the maternal/fetal blood volumes and the blood vessels are openly available at http://doi.org/10.5281/zenodo.4249627. The associated computational codes can be accessed at https://github.com/DiamondLightSource/python-placental-imaging. Additional data related to this paper may be requested from the authors.

REFERENCES

[1] R. M. Lewis and J. E. Pearson-Farr, "Multiscale three-dimensional imaging of the placenta," *Placenta*, 2020.

[2] K. P. Leiser R Kosanke G, "Human placental vascularization.," *Placenta basic Res. Clin. Appl.*, 1991.

[3] M. Ø. Thunbo *et al.*, "Postpartum computed tomography angiography of the fetoplacental macrovasculature in normal pregnancies and in those complicated by fetal growth restriction," *Acta Obstet. Gynecol. Scand.*, vol. 97, no. 3, pp. 322–329, Mar. 2018.

[4] R. Aughwane *et al.*, "Micro-CT and histological investigation of the spatial pattern of feto-placental vascular density," *Placenta*, vol. 88, pp. 36–43, Dec. 2019.

[5] T. O. Junaid, R. S. Bradley, R. M. Lewis, J. D. Aplin, and E. D. Johnstone, "Whole organ vascular casting and microCT examination of the human placental vascular tree reveals novel alterations associated with pregnancy disease," *Sci*

bioRxiv preprint doi: https://doi.org/10.1101/2020.12.07.411462; this version posted December 7, 2020. The copyright holder for this preprint (which was not certified by peer review) is the author/funder, who has granted bioRxiv a license to display the preprint in perpetuity. It is made available under aCC-BY 4.0 International license.

Rep, vol. 7, no. 1, p. 4144, 2017.

[6] R. Plitman Mayo, D. S. Charnock-Jones, G. J. Burton, and M. L. Oyen, "Three-dimensional modeling of human placental terminal villi," *Placenta*, vol. 43, pp. 54–60, 2016.

[7] B. A. M. Lisman, M. J. B. van den Hoff, K. Boer, O. P. Bleker, K. van Groningen, and N. Exalto, "The architecture of first trimester chorionic villous vascularization: a confocal laser scanning microscopical study," *Hum. Reprod.*, vol. 22, no. 8, pp. 2254–2260, Aug. 2007.

[8] A. Gough *et al.*, "Biologically Relevant Heterogeneity: Metrics and Practical Insights," *SLAS Discov. Adv. Sci. Drug Discov.*, vol. 22, no. 3, pp. 213–237, Jan. 2017.

[9] S. Uchida, "Image processing and recognition for biological images," *Dev. Growth Differ.*, vol. 55, no. 4, pp. 523–549, May 2013.

[10] A. R. Cohen, "Extracting meaning from biological imaging data," *Mol. Biol. Cell*, vol. 25, no. 22, pp. 3470–3473, Nov. 2014.

[11] O. E. Jensen and I. L. Chernyavsky, "Blood Flow and Transport in the Human Placenta," *Annu. Rev. Fluid Mech.*, vol. 51, no. 1, pp. 25–47, Jan. 2019.

[12] D. A. Nordsletten, S. Blackett, M. D. Bentley, E. L. Ritman, and N. P. Smith, "Structural morphology of renal vasculature," *Am. J. Physiol. Circ. Physiol.*, vol. 291, no. 1, pp. H296–H309, Jul. 2006.

[13] A. Skawina, J. A. Litwin, J. Gorczyca, and A. J. Miodoński, "The vascular system of human fetal long bones: a scanning electron microscope study of corrosion casts," *J. Anat.*, vol. 185 (Pt 2, no. Pt 2, pp. 369–376, Oct. 1994.

[14] M. I. Townsley, "Structure and Composition of Pulmonary Arteries, Capillaries, and Veins," *Comprehensive Physiology*. pp. 675–709, 01-Jan-2012.

[15] İ. Atli and O. S. Gedik, "Sine-Net: A fully convolutional deep learning architecture for retinal blood vessel segmentation," *Eng. Sci. Technol. an Int. J.*, 2020.

[16] P. Looney *et al.*, "Automatic 3D ultrasound segmentation of the first trimester placenta using deep learning," in *2017 IEEE 14th International Symposium on*

bioRxiv preprint doi: https://doi.org/10.1101/2020.12.07.411462; this version posted December 7, 2020. The copyright holder for this preprint (which was not certified by peer review) is the author/funder, who has granted bioRxiv a license to display the preprint in perpetuity. It is made available under aCC-BY 4.0 International license.

Biomedical Imaging (ISBI 2017), 2017, pp. 279–282.

[17] Z. Luo, Y. Zhang, L. Zhou, B. Zhang, J. Luo, and H. Wu, "Micro-Vessel Image Segmentation Based on the AD-UNet Model," *IEEE Access*, vol. 7, pp. 143402–143411, 2019.

[18] W. Xianchenga *et al.*, "Retina Blood Vessel Segmentation Using A U-Net Based Convolutional Neural Network," *Procedia Comput. Sci.*, 2018.

[19] M. Livne *et al.*, "A U-Net Deep Learning Framework for High Performance Vessel Segmentation in Patients With Cerebrovascular Disease," *Front. Neurosci.*, vol. 13, p. 97, Feb. 2019.

[20] M. Han *et al.*, "Automatic Segmentation of Human Placenta Images With U-Net," *IEEE Access*, vol. 7, pp. 180083–180092, 2019.

[21] P. Sadda, M. Imamoglu, M. Dombrowski, X. Papademetris, M. O. Bahtiyar, and J. Onofrey, "Deep-learned placental vessel segmentation for intraoperative video enhancement in fetoscopic surgery," *Int. J. Comput. Assist. Radiol. Surg.*, vol. 14, no. 2, pp. 227–235, 2019.

[22] F. Milletari, N. Navab, and S.-A. Ahmadi, "V-Net: Fully Convolutional Neural Networks for Volumetric Medical Image Segmentation," *2016 Fourth Int. Conf. 3D Vis.*, 2016.

[23] C. W. Hecksel *et al.*, "Quantifying Variability of Manual Annotation in Cryo-Electron Tomograms," *Microsc. Microanal.*, vol. 22, no. 3, pp. 487–496, Jun. 2016.

[24] J. L. James, G. S. Whitley, and J. E. Cartwright, "Pre-eclampsia: fitting together the placental, immune and cardiovascular pieces," *J. Pathol.*, vol. 221, no. 4, pp. 363–378, 2010.

[25] W. M. Tun, C. H. Yap, S. N. Saw, J. L. James, and A. R. Clark, "Differences in placental capillary shear stress in fetal growth restriction may affect endothelial cell function and vascular network formation," *Sci. Rep.*, vol. 9, no. 1, p. 9876, 2019.

[26] A. Erlich, G. A. Nye, P. Brownbill, O. E. Jensen, and I. L. Chernyavsky, "Quantifying the impact of tissue metabolism on solute transport in feto-placental microvascular networks," *Interface Focus*, vol. 9, no. 5, p. 20190021, Oct. 2019.

bioRxiv preprint doi: https://doi.org/10.1101/2020.12.07.411462; this version posted December 7, 2020. The copyright holder for this preprint (which was not certified by peer review) is the author/funder, who has granted bioRxiv a license to display the preprint in perpetuity. It is made available under aCC-BY 4.0 International license.

[27] G. J. Burton, A. W. Woods, E. Jauniaux, and J. C. P. Kingdom, "Rheological and Physiological Consequences of Conversion of the Maternal Spiral Arteries for Uteroplacental Blood Flow during Human Pregnancy," *Placenta*, vol. 30, no. 6, pp. 473–482, 2009.

[28] S. Perazzolo, R. M. Lewis, and B. G. Sengers, "Modelling the effect of intervillous flow on solute transfer based on 3D imaging of the human placental microstructure," *Placenta*, vol. 60, pp. 21–27, Dec. 2017.

[29] K. Alim, S. Parsa, D. A. Weitz, and M. P. Brenner, "Local Pore Size Correlations Determine Flow Distributions in Porous Media," Phys. Rev. Lett. vol. 119, no. 14, pp. 144501, Oct. 2017.

[30] N. S. Dellschaft *et al.*, "The haemodynamics of the human placenta in utero," *PLOS Biol.*, vol. 18, no. 5, pp. 1–21, 2020.

[31] P. Pearce *et al.*, "Image-Based Modeling of Blood Flow and Oxygen Transfer in Feto-Placental Capillaries," *PLoS One*, vol. 11, no. 10, pp. 1–22, 2016.

[32] I. L. Chernyavsky, L. Leach, I. L. Dryden, and O. E. Jensen, "Transport in the placenta: homogenizing haemodynamics in a disordered medium.," *Philos. Trans. A. Math. Phys. Eng. Sci.*, vol. 369, no. 1954, pp. 4162–4182, Nov. 2011.

[33] C. J. Roth *et al.*, "Dynamic modeling of uteroplacental blood flow in IUGR indicates vortices and elevated pressure in the intervillous space--a pilot study," *Sci. Rep.*, vol. 7, p. 40771, 2017.

[34] J. S. Choi *et al.*, "Fabrication of Porous Extracellular Matrix Scaffolds from Human Adipose Tissue," *Tissue Eng. Part C Methods*, vol. 16, no. 3, pp. 387–396, Jul. 2009.

[35] M. Song, Y. Liu, and L. Hui, "Preparation and characterization of acellular adipose tissue matrix using a combination of physical and chemical treatments," *Mol Med Rep*, vol. 17, no. 1, pp. 138–146, 2018.

[36] C. Torres-Sanchez, J. McLaughlin, and A. Fotticchia, "Porosity and pore size effect on the properties of sintered Ti35Nb4Sn alloy scaffolds and their suitability for tissue engineering applications," *J. Alloys Compd.*, vol. 731, pp. 189–199, 2018.

bioRxiv preprint doi: https://doi.org/10.1101/2020.12.07.411462; this version posted December 7, 2020. The copyright holder for this preprint (which was not certified by peer review) is the author/funder, who has granted bioRxiv a license to display the preprint in perpetuity. It is made available under aCC-BY 4.0 International license.

[37] S. Wang, L. Liu, K. Li, L. Zhu, J. Chen, and Y. Hao, "Pore functionally graded Ti6Al4V scaffolds for bone tissue engineering application," *Mater. Des.*, vol. 168, p. 107643, 2019.

[38] E. Palaiologou, P. Goggin, D.S. Chatelet, E.M. Lofthouse, C. Torrens, B.G. Sengers, J.K. Cleal , A. Page, R.M. Lewis. "Serial block-face scanning electron microscopy of erythrocytes protruding through the human placental syncytiotrophoblast". *J. Anat*. Vol. 231, no. 4, p. 634-637, 2017.

[39] D. Cunningham, R.J. Morgan, P.R. Mills, L.M. Nelson, P.G. Toner, M. Soukop, C.S. McArdle, R.I. Russell, Functional and structural changes of the human proximal small intestine after cytotoxic therapy, J Clin Pathol 38(3) (1985) 265-70.

[40] E.A. Bearce, D.T. Grimes, On being the right shape: Roles for motile cilia and cerebrospinal fluid flow in body and spine morphology, Semin Cell Dev Biol (2020).

[41] Dubey LK, Karempudi P, Luther SA, Ludewig B, Harris NL. Interactions between fibroblastic reticular cells and B cells promote mesenteric lymph node lymphangiogenesis. Nature communications. 2017 Aug 28;8(1):1-3.

[42] P. Brownbill, N. Sebire, E. V McGillick, S. Ellery, and P. Murthi, "Ex Vivo Dual Perfusion of the Human Placenta: Disease Simulation, Therapeutic Pharmacokinetics and Analysis of Off-Target Effects BT - Preeclampsia : Methods and Protocols," P. Murthi and C. Vaillancourt, Eds. New York, NY: Springer New York, 2018, pp. 173–189.

[43] Y. Tokudome *et al.*, "Layered Double Hydroxide Nanoclusters: Aqueous, Concentrated, Stable, and Catalytically Active Colloids toward Green Chemistry," *ACS Nano*, vol. 10, no. 5, pp. 5550–5559, May 2016.

[44] A. E. Gash, T. M. Tillotson, J. H. Satcher, J. F. Poco, L. W. Hrubesh, and R. L. Simpson, "Use of Epoxides in the Sol–Gel Synthesis of Porous Iron(III) Oxide Monoliths from Fe(III) Salts," *Chem. Mater.*, vol. 13, no. 3, pp. 999–1007, Mar. 2001.

[45] Z. D. Pešić, A. De Fanis, U. Wagner, and C. Rau, "Experimental stations at I13 beamline at Diamond Light Source," *J. Phys. Conf. Ser.*, vol. 425, no. 18, p. 182003, 2013.

bioRxiv preprint doi: https://doi.org/10.1101/2020.12.07.411462; this version posted December 7, 2020. The copyright holder for this preprint (which was not certified by peer review) is the author/funder, who has granted bioRxiv a license to display the preprint in perpetuity. It is made available under aCC-BY 4.0 International license.

[46] C. Rau, U. Wagner, Z. Pešić, and A. De Fanis, "Coherent imaging at the Diamond beamline I13," *Phys. status solidi*, vol. 208, no. 11, pp. 2522–2525, Nov. 2011.

[47] A. C. Kak and M. Slaney, *Principles of computerized tomographic imaging*. 2002.

[48] R. C. Atwood, A. J. Bodey, S. W. T. Price, M. Basham, and M. Drakopoulos, "A high-throughput system for high-quality tomographic reconstruction of large datasets at Diamond Light Source," *Philos. Trans. R. Soc. A Math. Phys. Eng. Sci.*, vol. 373, no. 2043, p. 20140398, Jun. 2015.

[49] M. C. Strotton *et al.*, "Optimising complementary soft tissue synchrotron X-ray microtomography for reversibly-stained central nervous system samples," *Sci. Rep.*, vol. 8, no. 1, p. 12017, 2018.

[50] E. Guo *et al.*, "Synchrotron X-ray tomographic quantification of microstructural evolution in ice cream – a multi-phase soft solid," *RSC Adv.*, vol. 7, no. 25, pp. 15561–15573, 2017.

[51] I. Luengo *et al.*, "SuRVoS: Super-Region Volume Segmentation workbench," *J. Struct. Biol.*, vol. 198, no. 1, pp. 43–53, 2017.

[52] O. Ronneberge, P. Fischer, and T. Brox, *U-Net: Convolutional Networks for BiomedicalImage Segmentation*. 2015.

[53] J. Howard and S. Gugger, "Fastai: A Layered API for Deep Learn," *information*, 2020.

[54] K. He, X. Zhang, S. Ren, and J. Sun, "Deep Residual Learning for Image Recognition," *2016 IEEE Conf. on492Computer Vis. Pattern Recognit. (CVP*, 2016.

[55] O. Russakovsky *et al.*, "ImageNet Large Scale Visual Recognition Challenge," *Int. J. Comput. Vis.*, vol. 115, no. 3, pp. 211–252, 2015.

[56] P. Brownbill *et al.*, "Denudations as paracellular routes for alphafetoprotein and creatinine across the human syncytiotrophoblast," *Am. J. Physiol. Integr. Comp. Physiol.*, vol. 278, no. 3, pp. R677–R683, Mar. 2000.

[57] H. Elias and D. M. Hyde, "An elementary introduction to stereology (quantitative microscopy)," *Am. J. Anat.*, vol. 159, no. 4, pp. 411–446, Dec. 1980.

bioRxiv preprint doi: https://doi.org/10.1101/2020.12.07.411462; this version posted December 7, 2020. The copyright holder for this preprint (which was not certified by peer review) is the author/funder, who has granted bioRxiv a license to display the preprint in perpetuity. It is made available under aCC-BY 4.0 International license.

[58] Rueden, C. T., Schindelin, J. & Hiner, M. C. et al. (2017), "ImageJ2: ImageJ for the next generation of scientific image data", BMC Bioinformatics 18:529, PMID 29187165, doi:10.1186/s12859-017-1934-z

[59] A. Baddeley and E. B. V. Jensen, *Stereology for Statisticians.* 2005.

[60] A. G. Oluwadebi, K. G. Taylor, and L. Ma, "A case study on 3D characterisation of pore structure in a tight sandstone gas reservoir: The Collyhurst Sandstone, East Irish Sea Basin, northern England," *J. Nat. Gas Sci. Eng.*, vol. 68, p. 102917, 2019.

[61] L. Zhang *et al.*, "The Investigation of Permeability Calculation Using Digital Core Simulation Technology," *Energies*, vol. 12, 2019.

[62] Y. Zhao, G. Zhu, C. Zhang, S. Liu, D. Elsworth, and T. Zhang, "Pore-Scale Reconstruction and Simulation of Non-Darcy Flow in Synthetic Porous Rocks," *J. Geophys. Res. Solid Earth*, vol. 123, no. 4, pp. 2770–2786, Apr. 2018.

[63] Coker, D. A. and Torquato, S. (1995). Extraction of morphological quantities from a digitized medium. *J Appl Phys*, 77(12):6087–6099.

[64] Doi, M. (1976). A new variational approach to the diffusion and the flow problem in porous media. *J Phys Soc Jpn*, 40(2):567–572.

[65] Erlich, A., Pearce, P.,Mayo, R. P., Jensen, O. E., and Chernyavsky, I. L. (2019). Physical and geometric determinants of transport in fetoplacental microvascular networks. *Sci Adv*, 5(4): eaav6326.

[66] Lu, B. and Torquato, S. (1990). Local volume fraction fluctuations in heterogeneous media. *J Chem Phys*, 93(5):3452–3459.